ADVANCED MATERIALS
www.advmat.de

Inorganic Double Helices in Semiconducting SnIP

*Daniela Pfister, Konrad Schäfer, Claudia Ott, Birgit Gerke, Rainer Pöttgen, Oliver Janka, Maximilian Baumgartner, Anastasia Efimova, Andrea Hohmann, Peer Schmidt, Sabarinathan Venkatachalam, Leo van Wüllen, Ulrich Schürmann, Lorenz Kienle, Viola Duppel, Eric Parzinger, Bastian Miller, Jonathan Becker, Alexander Holleitner, Richard Weihrich, and Tom Nilges**

Double helices are one of the most fascinating structures in nature.[1] The discovery of the structure of DNA by Watson and Crick in 1953 inspired scientists to manufacture and examine (double) helical structures of various compounds and almost all classes of materials.[2,3] In polymer science, a helical arrangement can be found for instance in polytetrafluoroethylene (PTFE), being a commonly used material nowadays.[4] Obviously, the (double) helix is a prominent building block frequently realized in organic and living systems, but a pure carbon free and atomic scale pendant in the inorganic world is unknown. Recently, theoretical calculations predicted the existence of a simple atomic chain double helix for LiP but such an arrangement has not been realized yet.[5a] LiP reported in the 1980s only contains a P-helix coordinated by lithium.[5b]

D. Pfister, Dr. K. Schäfer, C. Ott, M. Baumgartner, Prof. T. Nilges
Department of Chemistry
Technical University of Munich
Lichtenbergstr. 4, 85748 Garching b. München, Germany
E-mail: tom.nilges@lrz.tum.de

Dr. B. Gerke, Dr. O. Janka, Prof. R. Pöttgen
Institut für Anorganische und Analytische Chemie
Westfälische Wilhelms-Universität Münster
Corrensstr. 30, 48149 Münster, Germany

Dr. A. Efimova, A. Hohmann, Prof. P. Schmidt
BTU Cottbus-Senftenberg
Großenhainer Str. 57, 01968 Senftenberg, Germany

Dr. S. Venkatachalam, Prof. L. van Wüllen
Institut für Physik
Universität Augsburg
Universitätsstr. 1, 86159 Augsburg, Germany

Dr. U. Schürmann, Prof. L. Kienle
Technische Fakultät
Christian-Albrechts-Universität zu Kiel
Kaiserstr. 2, 24143 Kiel, Germany

V. Duppel
Max-Planck-Institut für Festkörperforschung
Heisenbergstraße 1, 70569 Stuttgart, Germany

E. Parzinger, B. Miller, J. Becker, Prof. A. Holleitner
Walter Schottky and Physics Department
Technical University of Munich
Am Coulombwall 4a, 85748 Garching, Germany

Prof. R. Weihrich
Institut für Materials Resource Management
Universität Augsburg
Universitätsstr. 1, 86159 Augsburg, Germany

DOI: 10.1002/adma.201603135

Several approaches have been tested to prepare inorganic double helical materials. Double helical selenium was found in traces using double-walled carbon nanotubes as a template.[6] On a nonatomistic nanometer to micrometer scale, helical arrangements of semiconductors such as CdTe/CdS[7,8] or metals as gold templated by DNA[9] have been realized. A more complex double helical compound composed by metal-oxo species such as $[(CH_3)_2NH_2]K_4[V_{10}O_{10}(H_2O)_2(OH)_4(PO_4)_7]\cdot 4H_2O$ is known.[10] Materials adopting an inorganic double helical structure promise excellent mechanical, electrical, and optical properties.[2] A double helical arrangement will lead to an improved strength or strain compared to linear chains or single helices and secondary attractive interactions between the two helices in a double helix can be the origin of interesting electronic properties. Despite of an intensive research for more than 60 years, a nontemplated, carbon-free double helical inorganic structure on an atomic scale did not exist so far.

Bulk SnIP was prepared phase pure (Figure S1, Supporting Information) on a gram scale in a fast and simple solid state annealing reaction from tin, phosphorus and tin tetraiodide. In order to systemize the description of SnIP we discuss the determination of bulk and nanosized properties separately. SnIP crystallizes monoclinically, in space group $P2/c$ (No. 13) containing $Z = 14$ units in the unit cell and lattice parameters of a = 7.934(2) Å, b = 9.802(3) Å, c = 18.439(9) Å, and β = 110.06(5)° (**Figure 1**). Two substructures of different elemental composition, a helical $^1_\infty[P^-]$ chain of phosphorus and a second helical $^1_\infty[SnI^+]$ chain are forming SnIP double helices of 0.98 nm diameter.

The single rods are either left (*M*-helix) or right-handed (*P*-helix) and thus have opposite chirality. Both sets of double helices are assembled in a pseudo-hexagonal arrangement of rods along the *a*-axis. Seven SnIP units per two chain windings are present in each rod resulting in a 7/2 helix.[11,12] In Herrmann–Mauguin notation, the symmetry of a separate *P*-helix fulfills the rod group $P7_42$ in very good approximation, while that of an *M* helix corresponds to $P7_32$. Rods of a given chirality are arranged in rows along the *b*-direction. Bond lengths within the helices of d(Sn-I) = 3.060(2) to 3.288(3) Å for the tin-iodide helix and of d(P-P) = 2.170(5) to 2.211(5) Å for the phosphorus helix are common and comparable to distances in 3D-bulk compounds such as $Sn_{24}P_{19.3}I_8$ or binary compounds.[13]

In order to understand the structure and physical properties of SnIP we examined the electronic structure and chemical

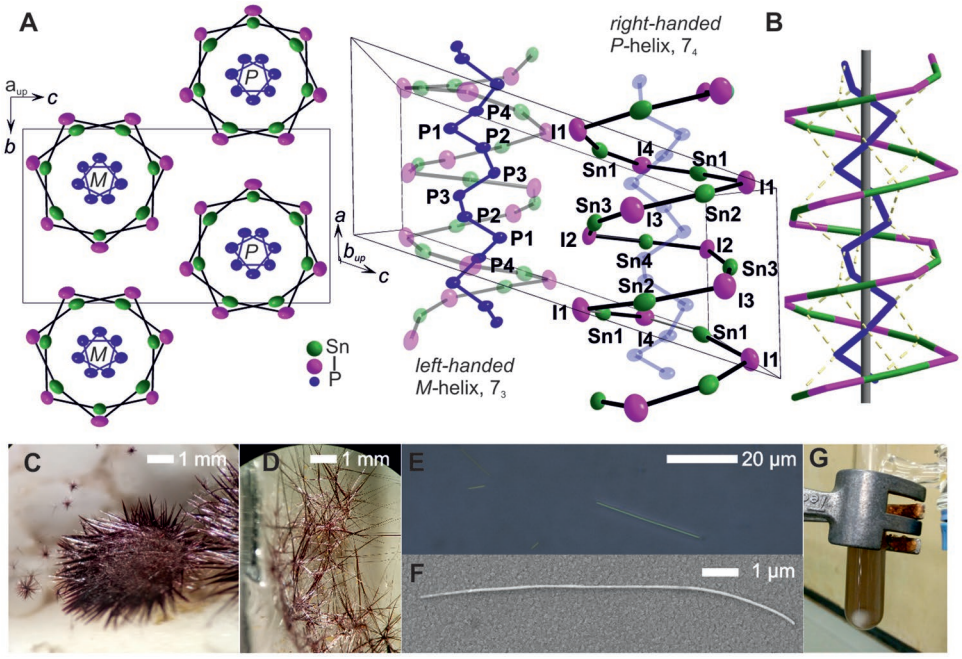

Figure 1. Bulk and nanosized crystals of double helical SnIP. A) Crystal structure sections projected along the *a* and *b* axis of SnIP. [SnI] and [P] helices are forming a double helical SnIP strand. B) Schematic representation of the double helix arrangement and the intrahelical Sn–P interaction. C,D) As-grown crystals of SnIP. E) Mechanically exfoliated SnIP on ITO presents different color shading under microscope dependent on thickness. F) Scanning electron microscopy (SEM) image of exfoliated SnIP on ITO with diameter 68 to 85 nm which indicates that it consists of multiple rods. G) Suspension of SnIP in chloroform.

bonding within and between the double helices in more detail (**Figure 2**). Quantum chemical calculations within the framework of DFT[14] were performed to envision the band structure and density of states (DOS) of SnIP. A graphical representation is given in Figure 2A,C.

Different functionals were applied for geometry optimization and energy calculations (see Supporting Information). GGA functionals with D2 correction for dispersion interactions have been selected as the best possible functional approach, based on previous observations on covalently bonded phosphorus allotropes[15] and 2D-layered materials[16] to describe all interactions including the weak van der Waals interactions in SnIP. Optimized[17] structure parameters are close to the observed ones with deviations smaller than 2% for the lattice parameters and of 3.5% for the cell volume. SnIP shows a calculated indirect band gap (hse06 functional) of 1.79 eV (between D_1 and Y_1 point) and a direct one of ≈1.81 eV (D_1 point). The indirect and direct optical band gap of SnIP have been determined experimentally by diffuse reflectance UV–vis spectroscopy as well as photoluminescence experiments (Figure 2G,H). We found an indirect band gap of 1.80 and a direct one of 1.86 eV for as-prepared bulk SnIP by UV–vis spectroscopy and 1.86 eV by photoluminescence. The calculated band gaps for bulk SnIP are in good agreement with the experimental ones. All calculations and experiments are fully consistent pointing toward an almost identical indirect and direct band gap.

To display the chemical bonding we performed an electron localization function (ELF) analysis of SnIP (see Figure 2F). The ELF shows two main features, the covalent character of the P–P bonds within the *P*-helices and the strong polarization of the Sn lone-pair, pointing toward the outer sphere of each SnI helix. A dative ionic interaction between the two helices can be assumed between the Sn and P atoms. Two lone pairs of phosphorus are pointing toward the tin positions resulting in bond lengths of *d*(Sn–P) = 2.669(3) to 2.708(3) Å.

The closest distance between the two SnIP double helices form two iodide ions with 3.738(3) Å. These attractive interactions between the single SnIP double helices are weak van der Waals (vdW) forces, which has direct consequences on the material properties. A binding energy of 25 kJ mol^{-1} was derived from density functional theory (DFT) calculations with D2 corrections taking van der Waals-like dispersion interactions (Figure S2, Supporting Information) into account. This rather weak interaction, significantly larger than in vdW systems like black P (7 kJ mol^{-1})[18] and H-bonding systems like in DNA, has consequences on the mechanical properties of SnIP. Bulk crystals with diameters of several micrometers can be bent 180° without visible disintegration (see Movie 1, Supporting Information). A more quantitative determination of the mechanical properties, like Young's modulus, are interesting and will be reported soon. We are optimistic that SnIP can be used in semiconductor-based applications like flexible optical devices due to its high mechanical flexibility, but one has to keep in mind that upon stress and strain the electronic properties can be affected. Obviously, the vdW interaction is strong enough to preserve the beneficial flexibility of double helices even in large scale crystals. On the other hand, the vdW interactions are weak enough to provide a certain cleavage tendency which was used for the fabrication of SnIP nanorods (see later on).

Adv. Mater. **2016**,
DOI: 10.1002/adma.201603135

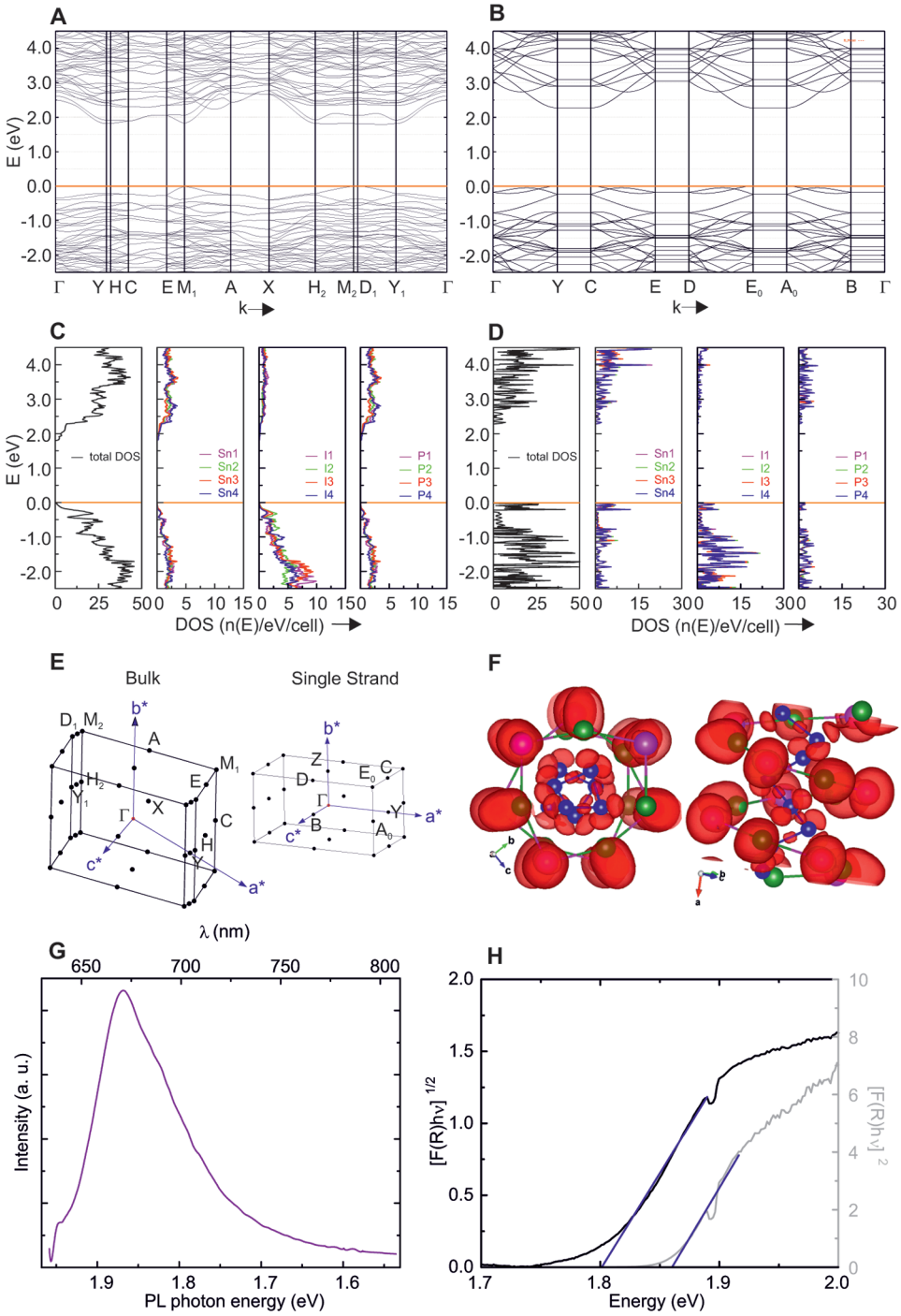

Figure 2. Electronic structure, density of states (DOS) and electronic properties of SnIP. A,C) Quantum chemical calculations within the DFT framework were performed for bulk and B,D) single rod SnIP. (A) The bulk and (B) the single rod band structure of SnIP. Band gaps are 1.79 and 2.27 eV, respectively. (C,D) The total DOS and partial DOS for 3D-bulk and single-rod SnIP. E) Corresponding Brillouin zones used for DFT calculations. F) Electron localization function (ELF) along and perpendicular to the rods show the covalent bonding between P, the dative, ionic Sn–P interaction and the polarized Sn(II) lone pair pointing toward the outside of the rod. G) Room temperature photoluminescence measurement on a SnIP needle featuring a minimum recombination energy of 1.86 eV with a shoulder at 1.8 eV. H) Diffuse reflectance UV–vis spectroscopy of micro crystalline SnIP. The Kubelka–Munk transformation was applied to determine the indirect band gap by extrapolation of $[F(R)h\nu]^{1/2}$ and direct band gap $[F(R)h\nu]^2$, respectively, versus the photon energy to zero absorption. The Tauc plot shows an indirect band gap of 1.8 eV and a direct band gap of 1.86 eV.

Additional structural, chemical, and physical properties of SnIP have been determined by various spectroscopic methods (Figures S3–S6, Supporting Information). ^{31}P-MAS-NMR and 2D-^{31}P RFDR (radio frequency driven recoupling) spectroscopy on 3D-bulk SnIP corroborate the P4-P1-P2-P3-P3-P2-P1-P4 connectivity pattern derived from single crystal structure

determination. Using ^{119}Sn Mößbauer spectroscopy the expected formal oxidation states of Sn^{2+}, I^-, and P^- were substantiated characterizing SnIP as an electron precise and diamagnetic compound. Measured Raman spectra show the characteristic vibration modes of P–P, Sn–P, and Sn–I bonds. We have assigned the modes to inter- and intrarod modes by the aid of quantum chemical calculations.[19]

SnIP starts to decompose at temperatures above 600 K by evaporation of SnI_4(g) and P_4(g) followed by SnI_2(g) to form the bulk residue (Figure S7b, Supporting Information). Only liquid tin remains after heating to 1000 K, and β-Sn was ultimately obtained as the solid phase after recrystallization. When tightly enclosed under its own vapor pressure, SnIP decomposes peritectically at 740(2) K with formation of $Sn_{24}P_{19.3}I_8$. A detailed phase diagram and a measurement of the equilibrium gas pressures above SnIP is given in the Supporting Information (Figure S7a,c, Supporting Information). The electrical conductivity was measured for a 500 nm crystal which will be reported in the oncoming nanosize part of the paper.

In the following we briefly discuss the preparation and properties of SnIP nanorods. As stated earlier on the inter-rod interactions of the SnIP double helices are weak enough to provide a cleavage tendency in bulk crystals. Bulk-SnIP can be mechanically and chemically delaminated into nanorods with large aspect ratios. Applying a commonly used Scotch-tape approach, crystals with micrometer diameters of bulk-SnIP (see Figure 1C,D) can be exfoliated down to ≈50 nm crystals within minutes. Representative crystals prepared by this approach are given in Figure 1E,F. Dependent on the number of shells coordinated around a single SnIP rod, different diameters can be expected (**Figure 3**A).

A single nanorod will show a diameter of 0.98 nm increasing to 9 nm for a rod surrounded by 4 shells (see Figure 3B). Bulk-SnIP can be suspended in different organic solvents such as toluene, *N*-methyl-2-pyrrolidone or chloroform; in the latter solvent within hours—if ultrasonication is applied, within minutes. The ability to suspend SnIP in organic solvents opens up perspectives for the fabrication of thin-layer devices with SnIP nanorods of variable lengths and diameters. As-prepared fibrous SnIP and nanosized rods are shown in Figures 1C,D and 3. SEM pictures (Figure 3C) illustrate the pronounced polymer-like morphology of SnIP. Aspect ratios larger than 500 were realized after successful delamination of bulky micrometer-sized SnIP crystals into nanometer rods. The thinnest rods observable by means of transmission electron microscopy (TEM) have a diameter of 15 nm (Figure 3B). Only the inner part of around 5 nm (or four SnIP shells) shows hereby residual crystallinity. The amorphous shell and the rounded shape of the rod end indicate the sensitivity of the material to the electron beam. Precession electron diffraction patterns (zone [010] in Figure 3D, and further in Figure S8, Supporting Information) coincide with the simulated patterns (Figure 3E) resulting from the suggested structure. High resolution images recorded in the same zone [010] at different focus values are shown in Figure 3F. The insets depict the simulation of the high resolution contrast and emphasize the agreement with the experimental data. An overlay of the structure in the high resolution simulation indicates the arrangement of the SnIP helices in the presented zone [010] and demonstrate the relation between contrast and structure (Figure 3G).

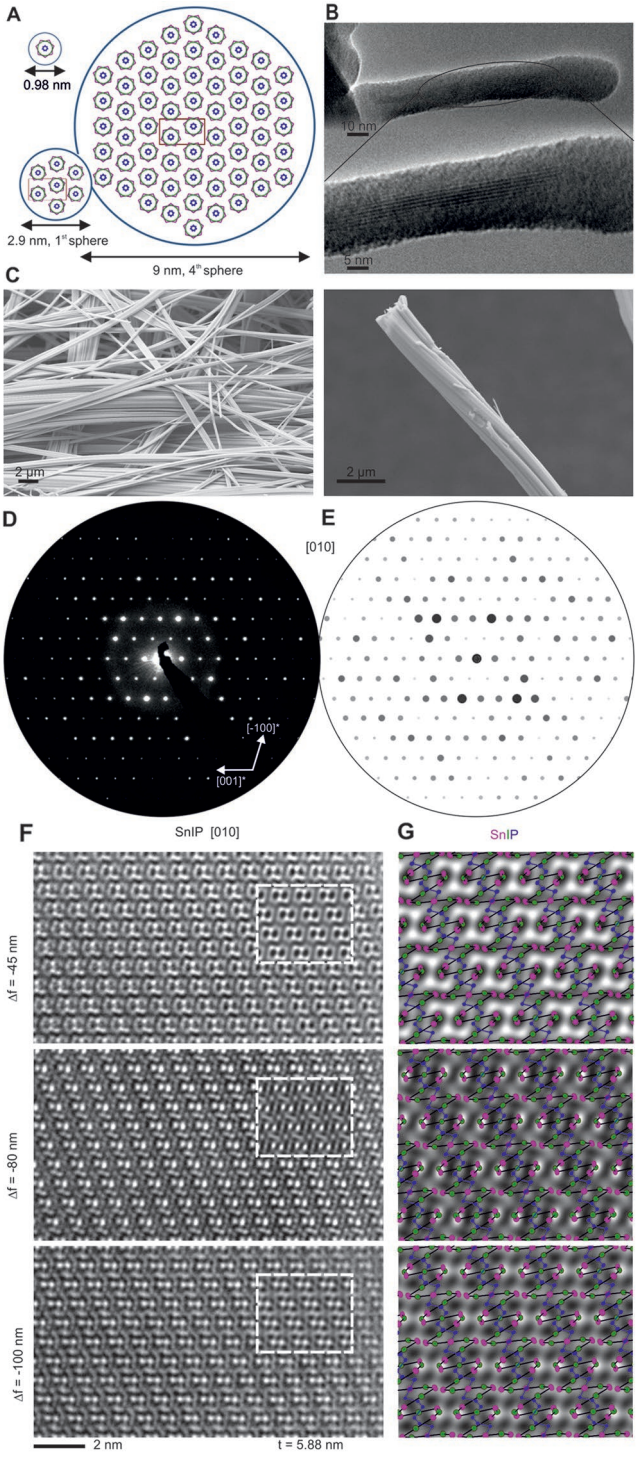

Figure 3. SnIP nanorods of different sizes and length scales. A) Schematic representation of SnIP nanorods starting from a single-rod to a four shell nanorod. B) TEM image of a thin rod with a diameter of 15 nm. C) SEM images of the SnIP rods. D) Precession electron diffraction (PED) pattern of the [010] zone with corresponding simulation (E). F) High resolution TEM images (zone [010]) at different focus values and insets showing simulations of the high resolution contrast. G) Overlay of the high resolution contrast simulations with the SnIP structure.

Adv. Mater. **2016**,
DOI: 10.1002/adma.201603135

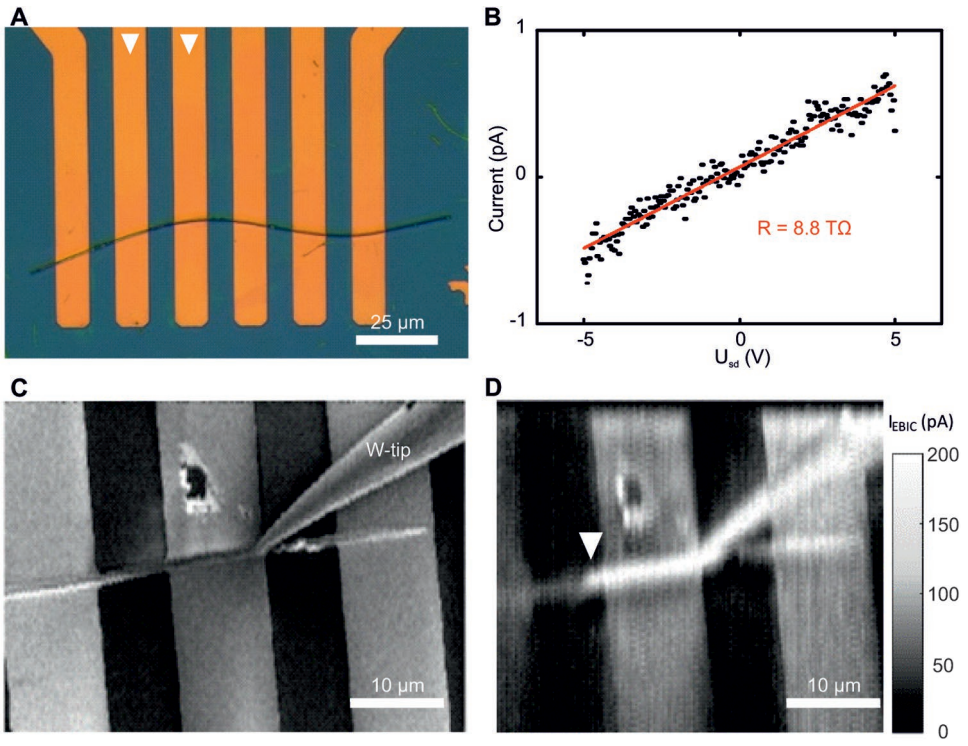

Figure 4. Electronic property measurements of SnIP. A) Optical microscope image of a SnIP-bundle contacted by six Ti/Au strips. The bundle is deposited on a Si/SiO_2-substrate. The SiO_2 (Ti/Au) has a thickness of 300 nm (3 nm/30 nm). B) Two-terminal current–voltage characteristic measured at the two strips highlighted by triangles in (A) with a preamplifier having an input resistance of 10 kΩ. C) Scanning electron microscope image of a similar SnIP-bundle which is additionally contacted by a tungsten tip (W-tip). The tip is positioned on top of the SnIP-bundle with the help of piezopositioners, and it is electronically connected to the current–voltage amplifier. Hereby, the electron beam induced current (EBIC) can be measured versus the position of the electron-beam. D) A corresponding EBIC-map at an acceleration voltage of 15 keV verifies that the current flow occurs across the contacted SnIP-bundle (e.g., triangle).

We also performed quantum chemical calculations for one double helical SnIP nanorod in order to evaluate the properties in more detail. After a geometry optimization and structure relaxation the structure remains almost unchanged (Figure S9, Supporting Information). Neither atomic distances nor the overall geometry change significantly going to the single nanorod. We calculated a band gap of 2.28 eV for a single SnIP nanorod which is larger than the value of 1.79 eV for the bulk material. Compared with a 2D-material like phosphorene where the 0.3 eV band gap of bulk black phosphorus is enlarged to >1.5 eV,[20] the band gap increase for bulk SnIP to single SnIP rod is only moderate. The small change of 0.49 eV from is in coincidence with the relative rigidity of the electronic structure. According our calculations, a quantum confinement has no drastic influence on the double helical SnIP structure itself. This finding is also substantiated by Raman spectroscopy. We found no significant differences in the calculated SnIP mode positions between bulk SnIP and a single nanorod (Figure S6, Supporting Information) which indicates an almost unaffected and noninfluenced stacking of single rods in the bulk material.

The conductivity of SnIP was estimated by electron beam induced current (EBIC) measurements (**Figure 4**) for a 500 nm SnIP crystal. A representative single crystal was mounted on a chip and contacted carefully. The crystal was bent several times prior to the conductivity measurement which resulted in a curved morphology. We observed an electronic conductivity of 2.5(5) µS m^{-1} which is comparable to 1 µS m^{-1} reported for nondoped GaAs.[21]

SnIP in its nanosized form can be regarded as a quantum confined semiconductor. Such semiconductors are widely used in energy science and technology. Examples are perovskite-based or all solid state dye-sensitized $CsSnI_3$ based solar cells which reach efficiencies larger than 10%.[22–25] Nanorod-polymer solar cells based on CdSe have been already produced underlining the potential of nanostructured semiconductors for energy conversion.[26] Furthermore, in most quantum dot applications of such kind toxic, less abundant, expensive elements, and often complex nanostructuring are needed to realize efficient materials. Bulk-SnIP as a 1.86 eV semiconductor contains nontoxic and abundant elements, which can be successfully delaminated mechanically and chemically to nanorods within minutes by state of the art techniques.[27] Even better, the measured direct band gap is relatively close to the efficiency maximum of single junction solar cells.[28] In the case of effective doping we are optimistic that the conductivity of SnIP can be optimized to make this material applicable.

The structural chemistry of double-helical SnIP is unique. While a 1:1:1 composition is the most prominent one in intermetallic systems such a composition is uncommon in main group chemistry. The general building principle of combining metal halides and complex building blocks can be found for the combination of copper halides and neutral polyphosphide

units[29] or bismuth polycations[30] in metal halide environments. Copper halide phosphorus adducts have been used as precursor compounds for the isolation of new phosphorus allotropes. One may ask the question if the single helices in SnIP might be separated from each other comparable with the neutral polyphosphide strands in the copper halide adducts. In contrast to the copper halide adducts both helices in SnIP are charged (see Table S2 of the Supporting Information for details) and it is therefore unlikely that both helices can be separated in an easy mechanical or chemical way.

The existence of double helical SnIP is unexpected and unusual but as novel prototype structure it offers perspective in nanoscience and related technologies. Double helical assemblies can be easily fabricated from organic substances due to their variable shapes and complex interactions while the inorganic counterpart is much more difficult to realize. The lack of directed inter and intramolecular interactions in the case of simple atom chains renders a self-assembly to pure inorganic double helices more challenging. On a larger scale, a double helical arrangement becomes more and more stable due to the increasing possibility of stabilization by secondary interactions. Several examples are known and only a small fraction will be discussed herein. Examples amongst others are silicon microtubes[31] or carbon nanotubes (CNT)[32] which show diameters of 10–50 µm and 4–6 nm (inner diameter of double-walled CNT), respectively. In the case of double helical CNT's,[33] a large quantity of unwanted byproducts (single helical or noncoiled rods) often disfavors such materials for applications. A combination of both strategies led to the formation of a double-helical Se rod in a double-walled CNT.[6,32] Templating or nanomolding[34] are widely used principles for materials design as shown for chiral Au-nanoparticle helices.[35] Glancing angle deposition were used to fabricate helical hollow Si nanotubes with 30 nm inner diameter.[36] Magnetite nanocubes can be arranged in helical superstructures on a post-atomic scale by an interplay of van der Waals and magnetic dipole–dipole interactions.[37] None of given examples are a purely inorganic carbon-free atomic double helix materials capable to be produced in a defined gram scale synthesis.

With SnIP, the first prototype representative of an atomic-scale double helical structure featuring a phosphorus $^1_\infty[P^-]$ and $^1_\infty[SnI^+]$ helix interpenetrating each other exists. A racemic mixture of left and right handed double helices is arranged parallel to each other, only bond by weak van der Waals interactions. As bulk material and as nanorods, SnIP shows an extraordinary flexibility and photoluminescence making it a promising candidate for semiconductor applications like flexible devices or in energy conversion processes. It can be synthesized phase pure in a simple process from the elements on a gram scale. Complex synthesis procedures or templating routes are not necessary and therefore up-scaling is possible. Due to the electronical and mechanical properties of SnIP a wide range of applications can be addressed in semiconductor science.[38] The pronounced 1D-character of SnIP and the simple production process of nanorods from bulk material defines a new and easily accessible 1D-substance class beside the well-established 2D-materials such as the molybdenum dichalcogenides, graphene or phosphorene. From a topological point of view the bonding situation of SnIP is comparable to the H-bond system in DNA.[39]

Experimental Section

Synthesis of Bulk and Nanostructured SnIP: SnI_4 was synthesized according to literature procedures.[40] A mixture of Sn (107.8 mg, 99,999%; Chempur), SnI_4 (189.6 mg, presynthesized as stated above), and red phosphorus (37.5 mg, ultrahigh grade, 99.999+%, Chempur) was pressed into a pellet (diameter 10 mm, 25 MPa for 15 min) and sealed in a silica glass ampoule under vacuum ($p < 10^{-3}$ mbar). The ampoule was placed in a Nabertherm muffle furnace (L3/11/330) with the starting materials located in the hot zone at 673 K. The melt was cooled down to room temperature within 75 h at the rate of 5 K h^{-1}. Single crystals were obtained by heating up to 923 K followed by slower cooling at the rates of 2 K h^{-1} to 773 K (holding period 15 h) and of 1 K h^{-1} to room temperature. The product has formed during cooling. SnIP can also be synthesized by heating the stoichiometric mixture of Sn, I_2, and red P in an evacuated ($p < 10^{-3}$ mbar) silica glass ampoule at 673 K for 10 h. The same cooling procedure was applied as described above. Bulk SnIP can be nanostructured either mechanically using tape (*Lensguard* 7568 by Nitto) or chemically by using chloroform, *N*-methyl-2-pyrrolidone or toluene. We used an ultrasonic bath with 45 kHz (80 W) for durations from 10 min to 10 h. The latter approach yields in nanorods with diameters smaller than 25 nm. The exfoliated products were examined with an optical light microscope from LEICA DM 1750 M (10 × 100 magnification).

Structure Determination: X-ray powder data were collected on a Stoe Stadi P diffractometer (Cu-$K_{\alpha1}$ radiation, λ = 1.54051 Å, Ge-monochromator) using a Mythen 1 K detector (Fa. Dectris). An external calibration was performed using Si (a = 5.43088 Å). Phase analysis and indexing was performed with the program package Stoe Winxpow.[41]

Single crystal data were measured with a Stoe IPDS II, equipped with Mo-K_α radiation (λ = 0.71073 Å) and a graphite monochromator. For SnIP, the absorption was corrected numerically, on the basis of symmetry equivalent reflections, after optimization of the crystal shape, using the Stoe *X-red* and X-shape programs.[42] The structure was solved by the Superflip routine[43] implemented in the Jana2006 program suite.[44]

Crystal Structure of SnIP: Stoe IPDS II diffractometer (MoK_α radiation, λ = 0.71069 Å), T = 293 K, crystal dimensions 0.03 × 0.05 × 0.3 mm^3, monoclinic, space group $P2/c$ (No. 13), lattice parameters a = 7.934(2) Å, b = 9.802(3) Å, c = 18.439(9) Å, β = 110.06(5)°, V = 1347.0(9) $Å^3$, Z = 14. ρ(calc.) = 4.77 g cm^{-3}, μ(MoK_α) = 14.8 mm^{-1}, numerical absorption correction[30], full matrix least squares refinement on F^2 using Jana2006 (32), 6796 reflections, 3567 unique ones, θ max = 29.13°, 98 parameters, R_{int} 0.086, $R1$(1651Fo >3σ(Fo)) = 0.0407, w$R2$ = 0.0840, GoF = 1.01, residual electron density +1.88/−1.98 e $Å^{-3}$.

Further details of the crystal structure investigation(s) may be obtained from the Fachinformationszentrum Karlsruhe, 76344 Eggenstein-Leopoldshafen (Germany), on quoting the depository number CSD-430054.

Scanning Electron Microscopy (SEM) and Energy Dispersive X-Ray Spectroscopy (EDS): SEM images and EDS were performed using a Jeol HR SEM JSM-7500F field emission scanning electron microscope with an Oxford Instrument Inca X-Max analyzer a Zeiss SII NVision40, and a Zeiss Ultra55Plus (Gemini, 5 kV). The EDS results were averaged from three different points selected randomly on the crystal surface. The acceleration voltage was set to 15 kV. The measured composition is in good agreement with the composition calculated from the structure refinement and by quantitative chemical analysis. No other impurities were detected.

Transmission Electron Microscopy: The SnIP needles suspended in butanol respectively prepared dry, were distributed onto grids and studied with different transmission electron microscopes: A Jem-2100 from Jeol (acceleration voltage 200 kV, LaB_6, spherical aberration coefficient C_S = 1.0 mm) with EDS detector (SDD, Oxford), a field emission gun microscope Tecnai F30 G2 from Fei (300 kV, C_S = 1.2 mm) with EDS detector (SiLi, Edax), and a Philips CM 30 ST microscope (300 kV, LaB_6 cathode, C_S = 1.15 mm) equipped with a spinning star device enabling the use of precession electron diffraction (PED)[45,46]

Adv. Mater. **2016**,
DOI: 10.1002/adma.201603135

in addition to selected area electron diffraction (SAED). Simulations of the SAED and PED pattern and the high resolution images were obtained with the JEMS software package.[47] The SnIP crystals grow as needles with different diameters. The analyzed crystals are beam sensitive. During recording of high resolution images the structure and morphology has changed. EDS measurements before and after recording of the images with focused beam longer than 1 min show also the change in the stoichiometry from the given Sn:I:P ratio of 1:1:1 to almost 3:1:3.

Quantum Chemical Calculations: All quantum chemical calculations were performed in the framework of DFT within the all-electron local orbital approach with the Schlegel algorithm as implemented in Crystal14.[14] For all structure optimizations on bulk (3D periodic) and single polymer (1D periodic) models the PBE functional with and without Grimme's D2 correction for vdW interactions[16] was performed. Electronic band structures were calculated with HSE06 functionals.[48,49] Energy versus volume curves were computed with the implemented EOS (equation of state) function. For all calculations including DOS, Sn Fermi contact density, and IR- and Raman frequencies all electron Gaussian type basis sets were applied for P (AE-531151d1*)[50] and Sn (AE-976631311d1*),[51] and a valence basis set for I (HW-1111111*).[52] All calculations were converged to k-point shrinking of $2 \times 2 \times 2$ to $8 \times 8 \times 8$. Graphical representations were created with Xcrysden.[53]

For the description of the SnIP rods we used two different models, a single strand and 1D-polymer. For both models we used the data from structure determination. For the single strand model the distance between the rods was increased to 8.3 Å. At this distance dispersion interactions between the SnIP rods are vanished. For the 1D-model the smallest building block of one strand in the unit cell was taken as repetitive unit and all crystal symmetry was removed. A translation was allowed in rod-direction only.

Thermal Analysis: Differential scanning calorimetry (DSC) was conducted on a DSC 404 *Pegasus* instrument (Netzsch). About 80 mg of the sample were sealed in a cylindrical niobium crucible by arc-welding in an argon-filled glovebox. An empty sealed crucible served as a reference. The measurements were performed under an argon flow of 60–70 mL min^{-1} with the heating rate of 10 mL min^{-1} up to 973 and 1273 K, respectively. The DSC data were processed with the Proteus Thermal Analysis software.[54]

Thermogravimetry (TG): The presented thermogravimetric data were recorded in the range from the ambient temperature to 1273 K with the heating rate of 10 K min^{-1} under nitrogen with the flow rate of 100 mL min^{-1} using a simultaneous thermal analyzer (STA 449 F3 Jupiter) manufactured by Netzsch. Additional experiments under argon atmosphere were performed using a simultaneous thermal analyzer STA 409 Luxx from Netzsch with the flow rate of 100 mL min^{-1} from ambient to 1673 K. In order to analyze the intermediate products of thermal decomposition, measurements from ambient to 730 and 743 K, respectively, were carried out on a STA 449 F3 Jupiter instrument with the heating rate of 2 K min^{-1} (end temperature: 730 K) and 10 K min^{-1} (end temperature: 743 K). The masses of SnIP taken for various measurements were ≈21 mg. The reported decomposition temperatures were determined at the onset of the differential thermogravimetry (DTG) curve of the respective thermal effect. In order to identify crystalline products of thermal decomposition, powder X-ray diffraction patterns were collected on a Bruker D2 X-ray diffractometer using the accelerating voltage of 30 kV and the filament current of 10 mA. The patterns were recorded with CuK_α radiation in the reflection mode by a LynxEye detector.

High Temperature Gas Balance: Thermal decomposition behavior of SnIP under its own equilibrium vapor pressure was analyzed using an advanced high-temperature gas balance (HTGB).[55] In this method, the vapor phase is enclosed in a silica ampoule and thus forms the equilibrium gas phase in permanent contact with the solid phase. The measured signal is evoked by the change of the leverage of the horizontal balance support during evaporation and condensation. Application of the HTGB method enables analysis of the solid–gas equilibria in the working range from 0.01 till 15 bars at temperatures up to 1373 K. For the present measurements the total mass of 199.5 mg of starting material SnIP was sealed in evacuated silica ampoules (V = 16 cm^3) and heated up with the rate of 10 K h^{-1} up to 1123 K, then and cooled down to ambient with the rate of 10 K h^{-1}.

Spectroscopic Studies: A $Ca^{119m}SnO_3$ source was used for the ^{119}Sn Mößbauer spectroscopic investigations. The sample was enclosed in a small thin-walled polymethyl metacrylate (PMMA) container at a thickness of about 13 mg Sn cm^{-2}. A palladium foil of 0.05 mm thickness was used to reduce the tin K X-rays concurrently emitted by this source. The measurement was conducted in the usual transmission geometry at ambient and liquid nitrogen temperature (bath cryostat). The Mößbauer source was kept at room temperature. Fitting of the data was done by using the Normos-90 program package.[56]

Raman Spectroscopy: Raman spectra were measured using a Senterra Spectrometer (Bruker Optics GmbH) equipped with a 785 nm laser and 1 mW power. The spectrum was gained by adding five separate measurements with an integration time of 30 s each and a magnification of 50× (slide 50 × 1000 µm, zoom lens 50 long distance).

^{31}P Nuclear Magnetic Resonance: Solid state ^{31}P NMR experiments were performed employing a Bruker Avance III spectrometer operating at 7 T at a resonance frequency of 121.53 MHz. MAS was performed using a Bruker 1.3 mm probe at spinning frequencies of 30 kHz, employing RF amplitudes of 122 kHz for ^{31}P. Chemical shifts are referenced to 85% H_3PO_4 with ammonium dihydrogen phosphate as an external standard. The ^{31}P-MAS-NMR spectrum of SnIP, obtained using a repetition time of 300 s, was deconvoluted with the help of the Dmfit software.[57] A 2D ^{31}P RFDR-NMR experiment,[58] which measures the homonuclear magnetic dipole coupling between the ^{31}P nuclei, was performed to trace the connectivity's between the P atoms present in the structure. For this experiment, a saturation comb (repetition time 30 s) was used for the excitation, the mixing time was set to 1.6 ms.

Diffuse-Reflectance UV–vis: Diffuse-reflectance UV–vis measurements of powdered and crystalline SnIP samples were performed with an Avantes Avaspec 2048 spectrometer and a deuterium/halogen light source (Avalight-DH-S-BAL) connected via a reflection probe (FCR-7UV200-2-ME) using a home-made sample holder (depth: 5 mm). DR UV–vis spectrum is plotted in the form of Kubelka–Munk[59] function defined as $F(R) = (1\text{-}R)^2\ (2R)^{-1}$ with $R = R_S/R_T$, where R_S is the reflectance of the sample and R_T is the reflectance of PTFE used as a reference. A Tauc plot ($[F(R)h\nu]^x$ with x = 0.5 for an indirect and x = 2 for a direct band gap) was used to derive the bandgap.[60,61]

Photoluminescence Spectroscopy: Photoluminescence on a SnIP needle was measured at ambient temperature on a Princton Instruments PyLoN LN Digital CCD Spectroscopy System with single grating of 1,800 1 mm^{-1}. A linear polarized He/Ne-laser (633 nm, 86 µW) is used to excite the SnIP wires. The spectrum was gained by integrating for 120 s using a 100x Zeiss LD EC Epiplan-Neofluar objective.

Magnetic Properties: SnIP was used either as a polycrystalline powder or as a compact piece. The polycrystalline sample was packed in PE capsules and attached to the sample holder rod of a vibrating sample magnetometer unit (VSM) for measuring the magnetization M(T) in a quantum design physical-property-measurement-system (PPMS). The compact piece was attached to the sample holder rod using Kapton foil. The samples were investigated in the temperature range of 3–300 K with magnetic flux densities up to 10 kOe.

Electronic Property Measurements: For the conductance measurements, SnIPs were transferred onto silicon substrates with a silicon dioxide layer of 300 nm on top. The contacts to the nanowires were made by optical lithography and e-beam evaporation of 3 nm Ti and 30 nm Au using the AZ 5214E photoresist and AZ 351 B developer provided by AZ Electronic Materials GmbH and a maskaligner from Karl Süss GmbH&Co. The evaporator is custom-built. The two-terminal current–voltage characteristic was measured at the two contacts highlighted by triangles in Figure S12A of the Supporting Information. A Yokogawa Electric Corporation DC source (Model 7651) was used to apply a bias between –5 and +5 V. The current was measured using a DL INSTUMENTS 1211 current preamplifier (10–9 A/V) together with an Agilent 34410A digital multimeter (Keysight Technologies). The electron

beam induced current (EBIC) measurement was performed using a Zeiss NVision40 scanning electron microscope. One end of the SnIP bundle was contacted by a tungsten tip attached to a micromanipulator from kleindiek nanotechnik. The current in and out of the probe tip was converted to voltage by a DL Systems 1211 current preamplifier (10–9 A/V) and sampled by a National Instruments PXI-DAQ system, along with the signal of the SEM in-lens detector. All data acquisitions were synchronized to the SEM scanning pattern by a dedicated timing module.

SnIP: mp 740 K (peritectic decomposition); ^{31}P Solid State NMR (121.53 MHz, 85% H_3PO_4, δ): 39.0 (P4), 25.3 (P1, P2), 10.5 (P3); Raman (785 nm laser): ν = 460 (w), 450 (w), 446 (w), 439 (w), 351 (w), 339 (w), 218 (w), 180 (vw), 129 (s), 109 (w), 101 (w), 90 (m), 85 (m), 74 (w), 67 (m), 63 (m); Analytical calculation for SnIP (in at%): Sn 33.3, I 33.3, P 33.3; found (EDS): Sn 34(1), I 33(1), P 33(1).

Supporting Information

Supporting Information is available from the Wiley Online Library or from the author.

Acknowledgements

T.N. and D.P. conceived the idea and initiated the study. C.O. and D.P. synthesized the samples under the supervision of T.N. All phase analytical and thermoanalytical measurements were performed by D.P., C.O., A.E., A. Hohmann, and P.S.M.B. and R.W. performed the DFT calculations. B.G. and R.P. measured the Mößbauer spectra. L.v.W. conducted the Solid State NMR spectra. O.J. and R.P. performed the magnetic measurements. U.S., L.K., and V.D. are responsible for the TEM measurements. E.P. and A. Holleitner measured the photoluminescence spectra and E.P., B.M., J.B., and A.Hol. the electrical conductivity. T.N. wrote the manuscript with feedback from all others. The authors thank Prof. Ulrich Müller for fruitful discussions and advices concerning the structure description; Prof. S. Berensmeier at TUM for using their Raman microscope; L. Scherf for DSC measurements; T. F. Berto and Prof. J. A. Lercher for diffuse reflectance measurements; K. Rodewald and Christin Szillus for SEM and EDX measurements. This work is funded by the DFG via Priority Research Program SPP 1415 and Grant Nos. SCHM 1616/3-2, WE 4284/3- and WU237/4-2, and within the International Graduate School ATUMS IRTG 2022. P.S. exceedingly thanks the team of Prof. Bornhäuser and Prof. Ehninger (medical clinic 1 in Dresden) for having preserved him alive. D.P., C.O., and M.B. thanks the TUM graduate School for financial support.

Received: June 14, 2016
Revised: July 27, 2016
Published online:

[1] J. D. Watson, F. H. Crick, *Nature* **1953**, *171*, 737.
[2] M.-Q. Zhao, Q. Zhang, G.-L. Tian, F. Wei, *Nanoscale* **2014**, *6*, 9339.
[3] C. Zeng, Y Chen, C. Liu, K. Nobusada, N. L. Rosi, R. Jin, *Sci. Adv.* **2015**, *1*, e1500425.
[4] C. W. Bunn, E. R. Howells, *Nature* **1954**, *174*, 549.
[5] a) A. S. Ivanov, A. J. Morris, K. V. Bozhenko, C. J. Pickard, A. I. Boldyrev, *Angew. Chem., Int. Ed.* **2012**, *51*, 8330; b) W. Hönle, H. G. von Schnering, *Z. Kristallogr.* **1981**, *155*, 307.
[6] T. Fujimori, R. B. dos Santos, T. Hayashi, M. Endo, K. Kanek, D. Tománek, *ACS Nano* **2013**, *7*, 5607.
[7] Z. Tang, Z. Zhang, Y. Wang, S. C. Glotzer, N. A. Kotov, *Science* **2006**, *314*, 274.
[8] S. Srivastava, A. Santos, K. Critchley, K. S. Kim, P. Podsiadlo, K. Sun, J. Lee, C. Xu, G. D. Lilly, S. C. Glotzer, N. A. Kotov, *Science* **2010**, *327*, 1355.
[9] J. Sharma, R. Chhabra, A. Cheng, J. Brownell, Y. Liu, H. Yan, *Science* **2009**, *323*, 112.
[10] V. Soghomonian, Q. Chen, R. C. Haushalter, J. Zubieta, C. J. O'Connor, *Science* **1993**, *259*, 1596.
[11] U. Müller, *Symmetry Relationships Between Crystal Structures: Applications of Crystallographic Group Theory in Crystal Chemistry*, Oxford University Press, UK **2013**.
[12] M. I. Aroyo, *International Tables for Crystallography, Volume A: Space Group Symmetry*, 6th ed., Springer, Germany **2016**.
[13] M. M. Shatruk, K. A. Kovnir, A. V. Shevelkov, I. A. Presniakov, B. A. Popovkin, *Inorg. Chem.* **1999**, *38*, 3455.
[14] R. Dovesi, R. Orlando, A. Erba, C. M. Zicovich-Wilson, B. Civalleri, S. Casassa, L. Maschio, M. Ferrabone, M. De La Pierre, P. D'Arco, Y. Noel, M. Causa, M. Rerat, B. Kirtman, *Int. J. Quantum Chem.* **2014**, *114*, 1287.
[15] a) F. Bachhuber, J. von Appen, R. Dronskowski, P. Schmidt, T. Nilges, A. Pfitzner, R. Weihrich, *Angew. Chem.* **2014**, *126*, 11813; b) F. Bachhuber, J. von Appen, R. Dronskowski, P. Schmidt, T. Nilges, A. Pfitzner, R. Weihrich, *Angew. Chem., Int. Ed.* **2014**, *53*, 11629.
[16] a) O. Osters, T. Nilges, R. Weihrich, F. Bachhuber, F. Pielnhofer, M. Schöneich, P. Schmidt, *Angew. Chem.* **2012**, *124*, 3049; b) O. Osters, T. Nilges, R. Weihrich, F. Bachhuber, F. Pielnhofer, M. Schöneich, P. Schmidt, *Angew. Chem., Int. Ed.* **2012**, *51*, 2994.
[17] K. Doll, R. Dovesi, R. Orlando, *Theor. Chem. Acc.* **2005**, *115*, 354.
[18] F. Bachhuber, J. von Appen, R. Dronskowski, P. Schmidt, T. Nilges, A. Pfitzner, R. Weihrich, *Z. Kristallogr.* **2015**, *230*, 107.
[19] C. M. Zicovich-Wilson, F. J. Torres, F. Pascale, L. Valenzano, R. Orlando, R. Dovesi, *J. Comput. Chem.* **2008**, *29*, 2268.
[20] L. Li, Y. Yu, G. J. Ye, Q. Ge, X. Ou, H. Wu, D. Feng, X. H. Chen, Y. Zhang, *Nat. Nanotechnol.* **2014**, *9*, 372.
[21] K. Terashima, T. Katsumata, F. Orito, T. Kikuta, T. Fukuda, *Jpn. J. Appl. Phys.* **1983**, *22*, L325.
[22] M. Graetzel, R. A. J. Janssen, D. B. Mitzi, E. H. Sargent, *Nature* **2012**, *488*, 304.
[23] W. Chen, Y. Wu, Y. Yue, J. Liu, W. Zhang, X. Yang, H. Chen, E. Bi, I. Ashraful, M. Grätzel, L. Han, *Science* **2015**, *350*, 944.
[24] W. Nie, H. Tsai, R. Asadpour, J. C. Blancon, A. J. Neukirch, G. Gupta, J. J. Crochet, M. Chhowalla, S. Tretiak, M. A. Alam, H. L. Wang, A. D. Mohite, *Science* **2015**, *347*, 522.
[25] I. Chung, B. Lee, J. He, R. P. H. Chang, M. G. Kanatzidis, *Nature* **2012**, *485*, 486.
[26] W. U. Huynh, J. J. Dittmer, A. P. Alivisatos, *Science* **2002**, *295*, 2425.
[27] J. N. Coleman, M. Lotya, A. O'Neill, S. D. Bergin, P. J. King, U. Kha, K. Young, A. Gaucher, S. De, R. J. Smith, I. V. Shvets, S. K. Arora, G. Stanto, H.-Y. Kim, K. Lee, G. T. Kim, G. S. Duesberg, T. Hallam, J. J. Boland, J. J. Wang, J. F. Donegan, J. C. Grunlan, G. Moriarty, A. Shmeliov, R. J. Nicholls, J. M. Perkins, E. M. Grieveson, K. Theuwissen, D. W. McComb, P. D. Nellist, V. Nicolosi, *Science* **2011**, *331*, 568.
[28] W. Shockley, H. J. Queisser, *J. Appl. Phys.* **1961**, *32*, 510.
[29] A. Pfitzner, *Chem. Eur. J.* **2000**, *6*, 1891.
[30] E. Ahmed, M. Ruck, *Coord. Chem. Rev.* **2011**, *255*, 2892.
[31] H. Morito, H. Yamane, *Angew. Chem., Int. Ed.* **2010**, *49*, 3638.
[32] Q. Zhang, M.-Q. Zhao, D.-M. Tang, F. Li, J.-Q. Huang, B. Liu, W.-C. Zhu, Y.-H. Zhang, F. Wei, *Angew. Chem., Int. Ed.* **2010**, *49*, 3642.
[33] S. Iijima, T. Ichihashi, *Nature* **1993**, *363*, 603.
[34] W. Sun, E. Boulais, Y. Hakobyan, W. L. Wang, A. Guan, M. Bathe, P. Yin, *Science* **2014**, *346*, 1258361.

[35] A. Kuzyk, R. Schreiber, Z. Fan, G. Pardatscher, E. M. Roller, A. Högele, F. C. Simmel, A. O. Govorov, T. Liedl, *Nature* **2012**, *483*, 311.
[36] Z. Huang, K. D. Harris, M. J. Brett, *Adv. Mater.* **2009**, *21*, 2983.
[37] G. Singh, H. Chan, A. Baskin, E. Gelman, N. Repnin, P. Král, R. Klajn, *Science* **2014**, *345*, 1149.
[38] D. Pfister, C. Ott, M. Baumgartner, K. Schäfer, R. Weihrich, T. Nilges, *EP15176311.7*, **2015**.
[39] N. Narayana, M. A. Weiss, *J. Mol. Biol.* **2009**, *385*, 469.
[40] a) S. Lange, P. Schmidt, T. Nilges, *Inorg. Chem.* **2007**, *46*, 4028; b) M. Köpf, N. Eckstein, D. Pfister, C. Grotz, I. Krüger, M. Greiwe, T. Hansen, H. Kohlmann, T. Nilges, *J. Cryst. Growth* **2014**, *405*, 6.
[41] *Stoe Winxpow, Version 3.0.2.1*, Stoe & Cie GmbH, Darmstadt, Germany **2011**.
[42] a) Stoe Xarea, version 1.56, Stoe & Cie GmbH, Darmstadt, Germay **2011**; b) X-Red32, Version 1.53, Stoe & Cie GmbH, Darmstadt, Germany **2009**; c) X-shape, Version 2.1, Stoe & Cie GmbH, X-Red32, Darmstadt, Germany **2009**.
[43] L. Palatinus, G. Chapuis, *J. Appl. Crystallogr.* **2007**, *40*, 786.
[44] V. Petříček, M. Dušek, L. Palatinus, *Z. Kristallogr.* **2014**, *229*, 345.
[45] U. Schürmann, V. Duppel, S. Buller, W. Bensch, L. Kienle, *Cryst. Res. Technol.* **2011**, *46*, 561.
[46] R. Vincent, P. A. Midgley, *Ultramicroscopy* **1994**, *53*, 27.
[47] P. A. Stadelmann, *Ultramicroscopy* **1987**, *21*, 131.
[48] J. P. Perdew, Y. Wang, *Phys. Rev. B* **1992**, *45*, 13244.
[49] A. V. Krukau, O. A. Vydrov, A. F. Izmaylov, G. E. Scuseria, *J. Chem. Phys.* **2006**, *125*, 224106.
[50] A. J. Karttunen, T. F. Fässler, M. Linnolahti, T. A. Pakkanen, *Inorg. Chem.* **2011**, *50*, 1733.
[51] J. Rothballer, F. Bachhuber, F. Pielnhofer, S. M. Schappacher, R. Pöttgen, R. Weihrich, *Eur. J. Inorg. Chem.* **2013**, 248.
[52] K. Doll, H. Stoll, *Phys. Rev. B* **1998**, *57*, 4327.
[53] A. Kokalj, *J. Mol. Graphics Modell.* **1999**, *17*, 176.
[54] *Netzsch Proteus Thermal Analysis V4.8.2*, Netzsch-Gerätebau GmbH, Selb, Germany **2006**.
[55] P. Schmidt, M. Schöneich, M. Bawohl, T. Nilges, R. Weihrich, *J. Therm. Anal. Calorim.* **2011**, *110*, 1511.
[56] R. A. Brand, *Normos 90-Mößbauer Fitting Program*, Universität Duisburg, Duisburg, Germany **2007**.
[57] D. Massiot, F. Fayon, M. Capron, I. King, S. Le Calvé, B. Alonso, J.-O. Durand, B. Bujoli, Z. Gan, G. Hoatson, *Magn. Reson. Chem.* **2002**, *40*, 70.
[58] A. E. Bennett, R. G. Griffin, J. H. Ok, S. Vega, *J. Chem. Phys.* **1992**, *96*, 8624.
[59] P. Kubelka, F. Munk, *Z. Tech. Phys.* **1931**, *12*, 593.
[60] J. Tauc, R. Grigorovici, A. Vancu, *Phys. Status Solidi* **1966**, *15*, 627.
[61] J. Tauc, *J. Mater. Res. Bull.* **1968**, *3*, 37.